X-RAY–ILLUMINATED STELLAR WINDS: OPTICALLY THICK WIND MODELS FOR MASSIVE X-RAY BINARIES

IAN R. STEVENS[1,2]
Laboratory for High Energy Astrophysics, NASA/Goddard Space Flight Center

ABSTRACT

In massive X-ray binary systems (MXRBs), such as Vela X-1, the accretion-powered X-rays from the neutron star will alter the dynamics of the line-driven stellar wind of the early-type primary, by changing both the thermal and the ionization structure of the wind material. In a previous paper, Stevens and Kallman investigated this effect, neglecting optical depth effects in the transfer of X-rays through the stellar wind material. In this paper we extend this work and calculate radiative force multipliers $M(t, \xi, N_H)$ that now depend on the column of attenuating material N_H, as well as the ionization parameter ξ. Optical depth effects tend to suppress the effects of X-ray ionization on the force multipliers. We have calculated a number of dynamical models for the winds of MXRBs with these force multipliers. In contrast to the optically thin models, we were able to find self-consistent dynamical solutions for reasonable values of the X-ray luminosity L_x. These solutions also reveal the presence of nonlinear mechanisms that affect the wind dynamics, whereby relatively small changes in the force multipliers can lead to large changes in the wind structure. The models find the existence of a self-consistent region of solution at an X-ray luminosity of $L_x \sim 10^{36}$ ergs s^{-1}, and suggest the possible existence of high-luminosity states.

Subject headings: stars: neutron — stars: winds — X-rays: binaries

1. INTRODUCTION

Massive supersonic stellar winds are a universal feature of early-type stars, the winds being predominantly driven by the line absorption of the star's radiation field by the wind material. Massive X-ray binary systems (MXRBs) comprise a very interesting and useful subset of early-type systems. These systems consist of an OB giant or supergiant with a strong stellar wind, and a neutron star (or indeed black hole) companion, which accretes material from the stellar wind, giving rise to a strong X-ray flux.

The X-rays from the neutron star provide both an active and a passive probe of the stellar wind. The X-ray attenuation that has been observed from such systems provides a measure of the column density of the wind, and from this, some estimates of the wind accretion law, and a measure of the degree of ionization in the wind material (Haberl, White, & Kallman 1989; Corcoran & Heap 1991). Also, the X-rays will alter the thermal and ionization structure of the wind material and, as a consequence, alter the wind dynamics. The stellar winds in MXRB systems can therefore provide insight into the structure of stellar winds from early-type stars in general, and into the interaction of X-rays with stellar wind material.

In addition to the X-ray attenuation, further insight into the structure of MXRB stellar winds can be obtained from the ultraviolet P Cygni profiles of stong resonance lines, such as C IV λ1550 and N V λ1240, observed with the *International Ultraviolet Explorer* (*IUE*) satellite. In early-type stars in general, these lines provide a good indication of general wind characteristics, such as mass-loss rate and terminal velocities (Howarth & Prinja 1989). In addition to this, phase-dependent variability in these lines, associated with the orbit of the neutron star, was qualitatively predicted to occur in MXRBs

(Hatchett & McCray 1977). This variability, dubbed the "Hatchett-McCray effect" is a result of the X-rays from the neutron star either removing or enhancing the abundance of the ions responsible for the P Cygni profiles (for example, C^{3+} or N^{4+}) from the region of the wind around the neutron star and thus partially suppressing or enhancing the formation of different portions of the P Cygni profile. In fact, one of the early achievements of the *IUE* satellite was to actually observe this effect in Vela X-1 (Dupree et al. 1980). More recently, quantitative attempts to reproduce theoretically the observed phase-dependent P Cygni variability have been moderately successful (McCray et al. 1984).

The formulation of Castor, Abbott, & Klein (1975, hereafter CAK) remains the basis for the current most successful theoretical description of early-type star winds. The original CAK theory has been subsequently modified and improved by Pauldrach, Puls, & Kudritzki (1986, hereafter PPK) and Friend & Abbott (1986) to include the effects of the finite disk of the star on the wind dynamics. Models calculated with the modified CAK theory are (in terms of global properties such as mass-loss rate $\dot{M}$ and wind terminal velocity v_∞) in excellent agreement with the observed values (Howarth & Prinja 1989). While the CAK model, which implicitly assumes that the stellar wind is time-independent and monotonically accelerating, cannot reproduce time-dependent features of the stellar winds of early-type stars, such as the narrow absorption components (Prinja & Howarth 1988), or the observed X-rays (Cassinelli & Swank 1983), the good agreement between the time-averaged observed properties of early-type stars and CAK–type theory suggests that the application of this model to MXRB systems is justified and will give reasonable estimates of the global behavior of such systems.

Several authors have indeed used CAK–type theory to investigate the wind structure of MXRBs. Friend & Castor (1982), for example, studied the two-dimensional structure of the stellar wind in an MXRB in the orbital plane by allowing

---

[1] NAS/NRC Research Associate.
[2] Present address: Institute of Astronomy, Madingley Road, Cambridge CB3 0HA, UK.

for the binary gravitational potential. This meant that the primary star became extended in the direction toward the companion star in a tidal bulge. As a consequence, the mass-loss rate from the primary was enhanced along the line of centers of the system. A similar approach has been adopted by Stevens (1988a) in his model of the eccentric binary X-ray transient A0538−66. Both of these models concentrated on the impact of a modified gravitational potential on the wind dynamics and completely ignored the effects of X-ray ionization, which is the subject of this paper.

Several attempts, of varying levels of complexity, have been made to include the dynamical effects of X-ray ionization. Ho & Arons (1987) developed a relatively simple analytic approach to the problem, introducing a simple force cutoff into their model to mimic the effects of X-ray ionization. Ho & Arons (1987) assumed that the wind of the primary star obeyed a standard wind velocity law [i.e., $v(r) = v_\infty(1 - R_*/r)^\beta$] up to a location close to the neutron star. At this point, the wind material was assumed to have become sufficiently ionized that no further radiative driving took place, and the wind material coasted at constant velocity from this point on. One major consequence of their model was that it predicted the existence of two stable luminosity states, namely, a high and a low X-ray luminosity solution. The applicability of this model will be further discussed in § 6.

In a more sophisticated vein, Blondin et al. (1990) have presented results of two-dimensional time-dependent hydrodynamic calculations of the wind structure in MXRBs. Blondin et al. (1990) used a force law which, in the absence of X-ray ionization, mimics the CAK expression. To account for the effects of X-ray ionization, Blondin et al. (1990), in a similar way to Ho & Arons (1987), assumed that the radiative force was unaffected up to a certain value of the ionization parameter ξ (see eq. [1]), at which point the force dropped to zero. Blondin et al. (1990) found that the X-ray ionization could disrupt the flow, leading to the formation of dense wakes around the neutron star which could give rise to the episodes of enhanced absorption.

MacGregor & Vitello (1982, hereafter MV), using a modified form of the CAK equations, made the first attempt to calculate self-consistent dynamical models of the winds in MXRB systems including the effect of X-ray ionization on the wind structure. However, there were a number of limitations to this work. First, the calculations were only one dimensional (namely, along the line of centers of the system); second, the radiative force from the primary was approximated with only a small number of lines, whereas the line force will be comprised of contributions from a large assemblage of transitions from a number of different ions, including some of the heavier elements such as Fe (Abbott 1982); and third, the models they calculated assumed that the transfer of radiation through the wind material was optically thin. As a consequence of their assumptions, MV found that at X-ray luminosities of $L_x \sim 10^{34}$ ergs s^{-1} the radiative line force was essentially extinguished and the wind ceased to flow. This value is significantly lower than that observed in actual MXRB systems, where L_x is usually 10^{36} ergs s^{-1} or greater (Conti 1978).

In an earlier paper, Stevens & Kallman (1990, hereafter Paper I) relaxed one of the simplifications made by MV, accounting for a much larger number of driving lines, utilizing the line list described by Abbott (1982). However, these calculations were still made assuming that the wind flow is optically thin to the X-rays from the neutron star. In Paper I we calcu-

lated radiative force multipliers $M(t, \xi)$ that were now functions of both the optical depth parameter t (as was the case in the CAK model; see eq. [3]) and the ionization parameter ξ, finding that even when ξ was relatively small, significant changes occurred in $M(t, \xi)$. Stevens & Kallman (1990) also used these force multiplier results to calculate the one-dimensional structure of stellar winds in MXRBs, finding that the X-rays would severely inhibit the radiative acceleration of wind material in the supersonic regime. They also found that no self-consistent dynamical solutions could be obtained for neutron star X-ray luminosities greater than 10^{35} ergs s^{-1}, once again significantly lower than observed in MXRBs, and suggested that this discrepancy might be a consequence of the optically thin approximation.

In this paper we extend Paper I to include both the optical depth effects in the force multiplier calculations and the dynamical solutions. In Paper I the CAK force multiplier $M(t)$ was extended to include ionization effects and became a function of both t and ξ. When optical depth effects are included, an additional dependency is introduced, namely, $M = M(t, \xi, N_H)$, with N_H being the column density of material blocking the X-ray flux, and the calculation of the new force multipliers constitutes a major portion of this work.

The paper is set out as follows; in § 2 the results of the force multiplier calculations as a function of t, ξ, and N_H are presented; in § 3 the theory of the modified CAK wind dynamics is extended to include both ionization and optical depth effects is discussed; dynamical results of wind structure calculations are presented in § 4 for the case of a single star and for optically thin binary models, and in § 5 for optically thick binary models; and in § 6 we summarize and discuss the relationship between these calculations and the observed behavior of MXRBs.

2. THE RADIATIVE FORCE MULTIPLIERS

In order to study the influence of X-ray ionization on the wind dynamics in MXRBs, within the context of CAK–type theory, it is necessary to develop two separate components; (1) the dynamical model to actually calculate the wind structure (§ 3), and (2) the radiative force multipliers that parameterize the degree of momentum coupling between the wind material and the stellar radiation field. In this section we will calculate these force multipliers $M(t, \xi, N_H)$, including X-ray ionization and optical depth effects.

In Paper I the force multipliers were calculated as a function of t and ξ, but no dependence on N_H was included, the material being assumed to be optically thin. The force multipliers derived here thus represent an extension of those presented in Paper I; accordingly, the technique for calculating them is very similar, and many of the details associated with their calculation will not be reproduced here.

As in Paper I, the force multipliers have been calculated using the line list described by Abbott (1982). This extensive line list contains gf values for over 250,000 transitions from 17,000 electronic levels, for the first 30 elements in the periodic table (i.e., H to Zn). The data in this line list are generally only for the first six stages of ionization (in some cases the first nine stages), and as in Paper I, it has been necessary to interpolate to obtain the gf values for the transitions of more highly ionized species. Paper I contains a detailed discussion of the method of interpolating the necessary values and errors in the force multipliers that might result, and it will not be repeated here.

2.1. *Scaling Laws for Optically Thick Material*

The photoionization code described by Kallman & McCray (1982) has again been utilized to find the ionization and thermal structure of the wind material. In Paper I the ionization and thermal structure were calculated assuming that the wind material was optically thin, in which case the value of the ionization parameter ξ (ergs cm s^{-1}), given by

$$\xi = \frac{L_x}{nr_x^2} , \qquad (1)$$

determines the thermal and ionic state of the gas. In equation (1), L_x is the X-ray luminosity of the neutron star (ergs s^{-1}), r_x is the distance from the neutron star (cm), and n is the atomic number density (cm^{-3}).

Note that the assumption that the ionization structure is determined only by the ionization parameter ξ is violated only at high densities ($n > 10^9$ cm^{-3}) by collisional suppression of dielectronic recombination (Kallman & McCray 1982). The collisional suppression of forbidden lines at lower densities ($n > 10^3$ cm^{-3}) also breaks this relationship, but because the forbidden lines never have a major effect on the state of the gas at stellar wind densities, the departures are minimal.

In this paper, we include a finite optical depth, and in such a situation the state of the wind material not only depends on ξ but will also have an additional dependence on the amount of material attenuating the X-ray source. Hatchett, Buff, & McCray (1976) have derived the form of the additional scaling parameter (which we shall term ϵ), which, along with the ionization parameter ξ, will determine the gas temperature and ionization structure for optically thick material. To derive the form of the additional parameter ϵ, Hatchett et al. (1976) assumed that the wind density law was given by power law, namely,

$$n = Kr_x^{-\gamma} , \qquad (2)$$

with K a constant and r_x the distance from the neutron star as before. From this, they derived that the additional scaling parameter ϵ for optically thick material is given by

$$\epsilon = L_x^{1-\gamma} n r_x^\gamma . \qquad (3)$$

Thus, for constant density material $\gamma = 0$,

$$\epsilon = L_x n = \xi(nr_x)^2 = N_H^2 \xi , \qquad (4)$$

where, in this case, $N_H = nr_x$. However, in the winds of MXRBs, the wind density will not be constant. The region we are most particularly concerned about in the calculations is the region internal to the orbit of the neutron star, lying upon the line of centers of the system. In this situation, the density will increase with increasing r_x, and for the purposes of this discussion we will assume that the density structure in this region can be approximated by a power law in r_x as in equation (2), with an exponent $\gamma \leq 0$. It is a simple matter to show that, given the form of the second scaling parameter ϵ in equation (3) and the power-law distribution described above, ϵ can always be reduced to a simple product of ξ and N_H to varying powers. While the wind density structure on the line of centers of the system, and, indeed, viewed in any direction, will likely not follow a power-law relationship, the analysis above strongly suggests that, as would be expected, the effect of the inclusion of a finite optical depth on the wind ionization and thermal structure can quite generally be parameterized in terms of two variables only, namely, ξ and N_H. From this, the force multi-

pliers can then be parameterized in terms of three variables, namely, ξ, N_H, and the CAK optical depth parameter t (see eq. [6]).

In practical terms, in order to calculate the thermal and ionization structure of wind material at specific values of ξ and N_H, we assume a cloud with constant density. Then, by adjusting the location of the inner and outer radii of the cloud, and using the radiative transfer code of Kallman & McCray (1982), the ionization and thermal structure of the wind material can be determined at each point for a grid of values of ξ and N_H. The wind structure at each set of values of (ξ, N_H) can then be used to calculate the force multiplier $M(t, \xi, N_H)$.

In general, a finite column density will reduce the degree of ionization of the wind material; the higher the column density N_H, the higher the attenuation of the ionizing spectrum and the lower the degree of ionization. This will mean that, given the general trend found in Paper I that the higher the degree of ionization the smaller the force multiplier, a finite value of N_H will tend to increase the force multiplier $M(t, \xi, N_H)$ for the same values of t and ξ over the optically thin case.

In this paper, as in Paper I, the force multipliers have all been calculated assuming that the radiation field of the primary can be represented by a 25,000 K, $\log_{10} g = 3.0$ stellar atmosphere (Kurucz 1979). For the neutron star a 10 keV bremsstrahlung spectrum has been assumed, appropriate for MXRB systems (White, Swank, & Holt 1983). Note that the force multiplier results are very insensitive to the actual value of $\log_{10} g$ (Abbott 1982). These parameters are designed to be approximately representative of the MXRB system Vela X-1 (Conti 1978). As in the calculations of McCray et al. (1984), a minimum temperature was set on the wind material in the ionization structure calculation, though in these calculations the minimum value was set to $T_{min} = 0.6T_*$ (Drew 1989). However, the force multipliers are not very sensitive to the precise value of T_{min}.

The radiative force multipliers are given by the summation of the forces from individual lines,

$$M(t, \xi, N_H) = \sum_{lines} \frac{\Delta v_D F_v}{F} \frac{1}{t} (1 - e^{-\eta t}) , \qquad (5)$$

where Δv_D is the Doppler width of the transition, F_v is the emitted flux from the primary star (ergs cm^{-2} s^{-1} Hz^{-1}), F is the integrated flux of the primary (ergs cm^{-2} s^{-1}), and η is a dimensionless line strength parameter, which accounts for the ionic and electronic level populations as well as the gf value for the transition. The dimensionless Sobolev optical depth parameter t is given by

$$t = \sigma_e v_{th} \rho \left(\frac{dv}{dr}\right)^{-1} , \qquad (6)$$

with σ_e the electron scattering coefficient (cm^2 g^{-1}) and v_{th} the thermal speed (cm s^{-1}), ρ the mass density of the wind material (g cm^{-3}), and v the wind velocity (cm s^{-1}). The optical depth for each individual line is then given by $\tau_L = \eta t$.

2.2. *Force Multiplier Results*

The radiative force multipliers $M(t, \xi, N_H)$ have been calculated on a grid of t-values in the range 10^{-8} to 10^0, values of the ionization parameter in the range $0-10^4$ ergs cm^{-2} s^{-1}, and values of the column density N_H in the range $0-10^{24}$ cm^{-2}.

In Figures 1a–1c the force multipliers $M(t, \xi, N_H)$ are shown for a variety of values of ξ and N_H. The three separate figures
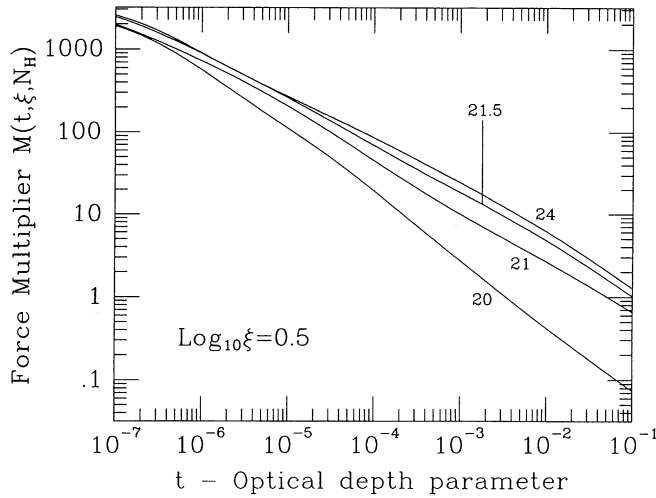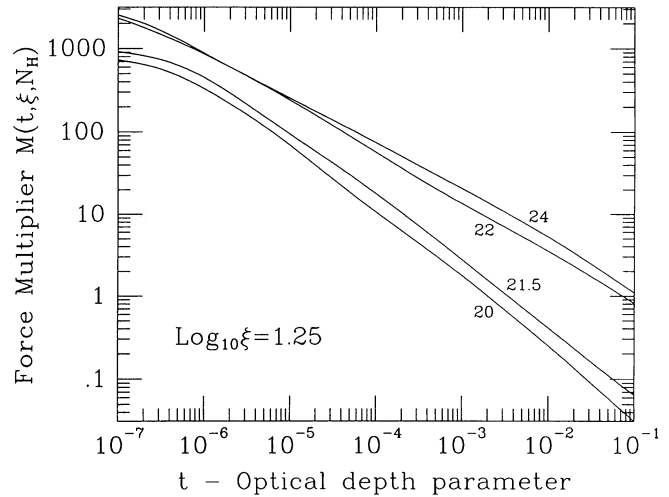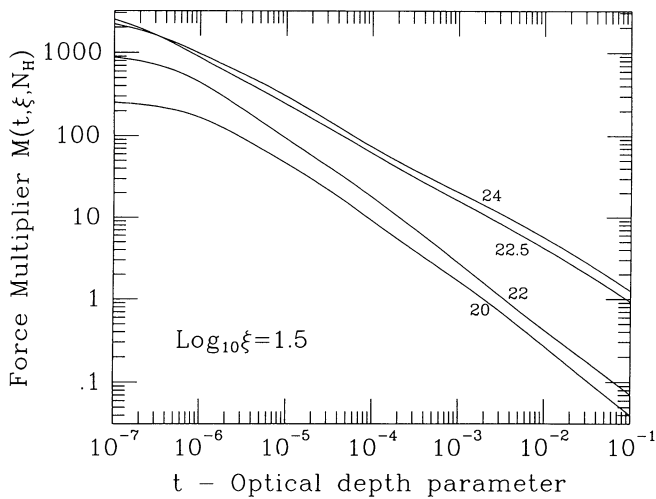
FIG. 1a

FIG. 1b

FIG. 1c

FIG. 1.—Variation of the radiative force multipliers $M(t, \xi, N_H)$ with increasing column density N_H, plotted as a function of the optical depth parameter t. Results are shown for three separate values of ξ. (a) For $\log_{10} \xi = 0.5$, the radiative force multipliers for four values of N_H are shown, namely, $\log_{10} N_H = 20, 21, 21.5$, and 24, the curves being labeled with the appropriate value of $\log_{10} N_H$. (b) Same as (a), but for $\log_{10} \xi = 1.25$ and for values of $\log_{10} N_H = 20, 21.5, 22$, and 24. (c) Same as (a), but for $\log_{10} \xi = 1.5$ and for values of $\log_{10} N_H = 20, 22, 22.5$, and 24.

are each for a different value of ξ, namely, $\log_{10} \xi = 0.5, 1.25$, and 1.5. In each figure, the force multiplier is plotted for four distinct values of N_H (which are not the same in each figure; see the figure captions for more details).

Two general trends can be seen from Figures 1a–1c. The first is that the force multipliers decline with increasing ξ (this is better illustrated in Fig. 2; see below). The second is that the force multipliers tend to increase with increasing N_H, though the details of the change are markedly different at the various values of ξ. In both cases, the changes are more pronounced at larger values of t.

The basic physical reason behind the decline in $M(t, \xi, N_H)$ with increasing ξ is the same as the process described in Paper I. For single-star models Abbott (1982) has calculated the force multiplier as a function of the effective temperature T_{eff} of the star, finding that $M(t)$ was largely insensitive to T_{eff}, for a wide range of values of T_{eff}. This is because the radiation field of the primary determines the ionization balance of the wind material, and this in turn determines the force multiplier. In the winds of OB stars the dominant ionization state of an element tends to have an ionization potential of around $20kT–30kT$, T being the wind temperature (i.e., $T \sim T_{eff}$), and the major resonance lines of these species typically lie at energies of around $5kT–7kT$. However, the maximum of the function νB_ν (cf. eq. [5]) occurs at around $4kT$, and this correlation tends to keep the force multiplier remarkably constant. However, in an MXRB, this is not necessarily the case; at higher values of ξ the ionization and thermal structure of the wind are determined by the radiation field of the neutron star. Thus, in MXRBs the wind material will always be overionized compared with the case of a single star, and this generally leads to ionic species dominating in the wind which tend to have their strongest lines at energies considerably higher than the stellar flux maximum point. Thus, X-ray ionization has a tendency to diminish the radiative line force.

For all three values of ξ shown in Figures 1a–1c, for $N_H \leq 10^{20}$ cm^{-2}, the force multipliers do not significantly depart from the optically thin case. Also, for $N_H \geq 10^{23}$ cm^{-2} the force multipliers show little change, and are unaffected by further increases in N_H, the attenuation being sufficient to block out the vast majority of the softer X-ray photons which can efficiently photoionize the wind material. However, for intermediate values of N_H the value of the force multiplier is a sensitive function of N_H, and the variation with N_H is different for the three values of ξ shown in Figures 1a–1c. For example, for $\log_{10} \xi = 0.5$, between $N_H = 10^{20}$ cm^{-2} and $N_H = 10^{21}$ cm^{-2}, the force multipliers increase by over an order of magnitude for some values of t, while for values of N_H between $10^{21.5}$ cm^{-2} and 10^{24} cm^{-2} only comparatively small ($\leq 30\%$) changes occur. A similar pattern occurs for $\log_{10} \xi = 1.25$. For values of $N_H \leq 10^{21.5}$ cm^{-2} only small changes occur with increasing N_H. In contrast, between $N_H = 10^{21.5}$ cm^{-2} and $N_H = 10^{22}$ cm^{-2} major changes occur with $M(t, \xi, N_H)$, increasing by more than an order of magnitude for some values of t. Then, for values $N_H \geq 10^{22}$ cm^{-2}, once more, only small changes occur in the force multipliers, the value of $M(t, \xi, N_H)$ changing by less than 50% for all t between $N_H = 10^{22}$ cm^{-2} and $N_H = 10^{24}$ cm^{-2}. For $\log_{10} \xi = 1.5$ again the behavior is similar, except that the major changes in this case occur

between $N_H = 10^{22}$ cm^{-2} and $N_H = 10^{22.5}$ cm^{-2}, with the changes at other values of N_H being much much smaller.

The behavior of the force multipliers $M(t, \xi, N_H)$ with increasing N_H is a consequence of the changing ionization balance (and to a lesser extent the changing thermal structure). For example, for $\log_{10} \xi = 1.25$, for smaller values of N_H, helium is predominantly in the form of He III, and for the heavier elements the dominant species are C V or C VI for carbon, or O V, O VI, or O VII for oxygen. For $\log_{10} \xi = 1.25$ fully ionized helium recombines to He II at a column density of around $\log_{10} N_H = 21.5$. The recombination of helium leads to a sharp increase in the opacity of the wind material, which in turn, prompts a rapid recombination of the heavier elements. Thus, when $N_H \geq 10^{22}$ cm^{-2}, the dominant species are then He II and either singly or doubly ionized species of C, N, and O. In this region, the optical depth in the energy range of the ionization edges of the species present in the gas is extremely high, and the influence of the X-rays on the ionization balance has been very significantly reduced by this attenuation. For the other values of ξ illustrated in Figure 1, the cause of the variation in the force multipliers with increasing N_H is the same, the difference being largely related to the location of the helium ionization edge (see Fig. 3). So for $\log_{10} \xi = 0.5$ the helium front occurs at a value of $N_H \sim 4 \times 10^{20}$ cm^{-2}, while for $\log_{10} \xi = 1.5$ the ionization edge occurs at around $N_H \sim 2.5 \times 10^{22}$ cm^{-2}.

In Figure 2 the force multipliers $M(t, \xi, N_H)$ are plotted as a function of the ionization parameter ξ and N_H for two specific values of t ($t = 10^{-4}$ and $t = 10^{-2}$). For other values of t the force multipliers behave in an analogous manner. For each value of t the force multipliers are plotted for six values of the column density N_H, namely, $\log_{10} N_H = 18, 20, 21, 21.5, 22$, and 22.5. The most obvious result from Figure 2 is that the force multipliers tend to decrease with increasing ξ, though now the form of the decrease of $M(t, \xi, N_H)$ with ξ is a strong function of N_H. The results for the lowest value of the column density shown ($N_H = 10^{18}$ cm^{-2}) essentially mimic the optically thin results presented in Paper I. At lower values of the column density N_H, the force multipliers $M(t, \xi, N_H)$ show a

marked decline at low values of ξ. For the case $t = 10^{-2}$ and $N_H = 10^{18}$ cm^{-2}, when the ionization parameter $\log_{10} \xi = 0$, the force multiplier has declined by close to an order of magnitude. The effect of higher column densities is to postpone the decline in $M(t, \xi, N_H)$ until increasingly higher values of ξ, and then for the force multipliers to drop sharply with further increases in ξ. Thus, for $N_H \geq 10^{22}$ cm^{-2}, for values of the ionization parameter below $\log_{10} \xi \leq 1$, only very small variations occur in $M(t, \xi, N_H)$ with increasing ξ. However, for $\log_{10} \xi$ in the range 1.5–2.0 the force multipliers drop reasonably quickly. The actual value of ξ where this sharp decline in $M(t, \xi, N_H)$ occurs depends on the value of N_H. The major underlying cause for this behavior is related to the helium ionization edge (see below). Note that while major changes occur close to the helium ionization front, later we shall see that the smaller changes that occur throughout the He II region have a very important dynamical impact (§ 5), and the changes in the force multipliers should not be considered as a step function at the helium edge.

For values of $\log_{10} \xi \geq 2$ the inclusion of optical depth effects does not significantly alter the force multipliers, until extremely high values of N_H. For values of ξ this high the wind material is basically completely ionized and is thus virtually transparent to the ionizing radiation field. Also, in regimes where such high values of ξ are appropriate, the dynamics tend to be dominated by the gravitational potential of the neutron star (see § 5).

2.3. The Helium Ionization Edge

The relationship between the decline in the force multipliers and the ionic state of the wind material can be better understood by considering the ionic state of helium. To do this we use a much simplified version of the ionization balance equation. For helium, the following equation approximately holds for its ionization structure;

$$\frac{n_2(r_x)}{4\pi r_x^2} \int_{E_T}^{\infty} \frac{L_x}{E_c} e^{-E/E_c} e^{-\tau(E)} a_2(E) \frac{dE}{E} = n_3(r_x) n_e(r_x) \alpha_3(T) , \quad (7)$$

where n_2 and n_3 are the respective ionic abundances of He II and He III (cm^{-3}) as a function of the distance from the X-ray source r_x (cm), n_e is the electron density (cm^{-3}), E_T is the threshold energy of He II ($E_T = 54$ eV), E_c is the characteristic energy of the bremsstrahlung spectrum of the neutron star (in this case $E_c = 10$ keV). The He II photoionization cross section $a_2(E)$ (cm^{-2}) can be approximated by $a_2(E) = a_0(E/E_T)^{-3}$, with $a_0 = 1.98 \times 10^{-18}$ cm^{-2}, and the He III to He II recombination rate α_3 (cm^3 s^{-1}) can be approximated by $\alpha_3 = 1.95 \times 10^{-12}$ $(T/eV)^{0.7}$ (Masai 1984). The energy-dependent optical depth $\tau(E)$ is given by

$$\tau(E) = \int_0^r n_2(r) a_2(E) dr . \quad (8)$$

While a reasonable approximation to the gas temperature T can be readily calculated (Masai 1984), for the purposes of this simplified discussion it is sufficient to use the results of Kallman & McCray (1982).

For the situation being considered here, equation (7) is valid, for the following reasons: (1) photoionization dominates over collisional ionization, (2) hydrogen is almost completely ionized and does not contribute significantly to the opacity, and (3) the heavier elements do not contribute strongly to the opacity in the energy regimes appropriate to helium photoion-
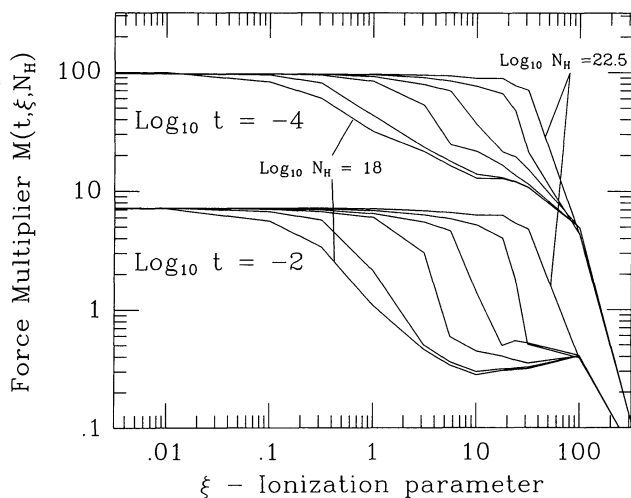

FIG. 2.—Radiative force multiplier $M(t, \xi, N_H)$ as a function of the ionization parameter ξ. The force multipliers shown are for values of $t = 10^{-4}$ and $t = 10^{-2}$, and are plotted for six values of N_H, namely, $\log_{10} N_H = 18, 20, 21, 21.5, 22, 22.5$. The force multipliers for the highest and lowest values of N_H are labeled with their respective values of $\log_{10} N_H$.
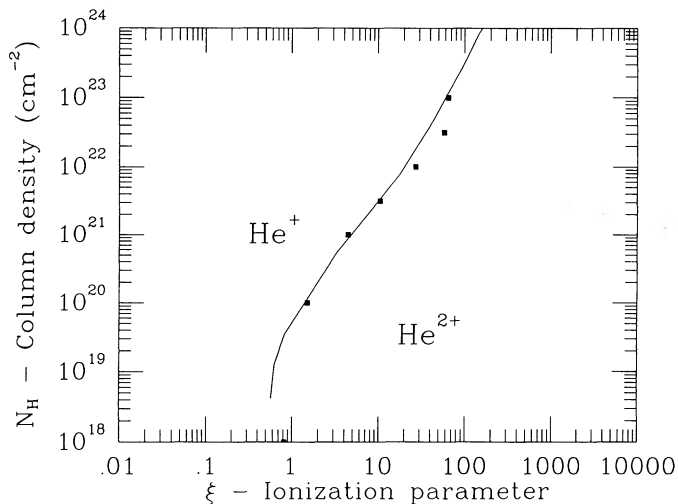
FIG. 3.—Helium ionization edge. The location of the point where the ionic abundances of He II and He III are equal is plotted as a function of ξ and N_H (solid line). Also plotted are the points where the force multipliers $M(t, \xi, N_H)$ for the case $t = 10^{-4}$ have fallen by a factor e from their maximum values at $\xi = 0$ (squares).

ization. The ionization balance for helium calculated with equation (7) agrees well with the much more detailed calculations used to actually calculate the force multipliers.

It is possible then to integrate equations (7) and (8) to find the location of the He II to He III ionization edge (defined to be the location where $n_2 = n_3$) as a function of both ξ and N_H, and some results are shown in Figure 3. For the optically thin limit, and, indeed, for small values of N_H, the helium edge occurs at relatively small values of ξ, with $\log_{10} \xi < 0$ (cf. Kallman & McCray 1982). As N_H increases, the location of the ionization edge moves to higher and higher values of ξ. For example, at a value of $N_H = 10^{22}$ cm^{-2}, the helium ionization edge occurs at a value of $\log_{10} \xi \sim 1.3$. The increase in the amount of attenuation of the X-ray flux requires a corresponding increase in the level of the unattenuated flux to maintain the same degree of ionization.

Also plotted in Figure 3 are the locations of the points in the (ξ, N_H)-plane where the force multipliers $M(t, \xi, N_H)$ (for a value of $t = 10^{-4}$, though the behavior is very similar at other values of t) have fallen by a factor e from their maximum values, which occur when there is no X-ray ionization, at $\xi = 0$. Figure 3 clearly shows the close coupling between the helium ionization edge and the decline in the force multipliers seen in Figure 2. However, the reason for the decline in $M(t, \xi, N_H)$ is not a direct consequence of the removal of He II ions, helium contributing little to the overall force multipliers (see Paper I). The reason is that the ionization structure of heavier elements is closely tied to that of helium. Once helium starts to recombine to He II, the opacity sharply increases over a large energy range, causing the heavier elements to recombine to lower stages of ionization. As noted above, the force multiplier is not a simple step function, and while the helium ionization edge marks a sharp change in $M(t, \xi, N_H)$, changes in the force multiplier that occur within the He II region will have important dynamical consequences (§ 5).

Another important point is that in optically thin models the ionization fronts are spread out over a large range in ξ, while, in contrast, for the optically thick models the ionization fronts are spread over a much smaller range in ξ. So for the case when

N_H is small, the decline in $M(t, \xi, N_H)$ with respect to ξ tends to be more gradual than for the cases when N_H is large. The differences between the optically thin and thick cases and the importance of the helium ionization edge on the overall ionization structure are well illustrated in the models of Kallman & McCray (1982).

With these force multipliers, the next step is to develop a modified version of the CAK model to self-consistently include X-ray ionization and optical depth effects, and the mathematical theory of this model is developed in § 3.

3. IMPROVED CAK THEORY FOR MXRB SYSTEMS

The model considered here is of an MXRB system, consisting of an early-type OB supergiant primary star of mass M_*, with a neutron star companion of mass M_x, the two stars being separated by a distance D. The dynamical model derived in this section includes the effects of X-ray heating and ionization and, in addition, the effects of a finite optical depth for the transfer of X-rays through the wind material. As such, it represents an advance over previous models that have neglected optical depth effects entirely, or have included them in an ad hoc manner.

The calculations presented here will be restricted only to the line of centers of the binary system. While it is desirable to extend the calculations into a second dimension, many of the physical processes at work can still be explored in a one-dimensional calculation. In addition, the extension to include optical depth effects in two dimensions, while conceptually relatively simple (for example, Stevens, Blondin, & Kallman 1990), would add very significantly to the computer time required.

While the basic equations used in this paper are similar to those used previously to model the winds of early-type stars and MXRBs (cf. Friend & Castor 1982; PPK), the fact that the radiative force multipliers are now a function of both the ionization parameter ξ and the column density N_H, in addition to the optical depth parameter t, significantly complicates the problem. However, some of the main characteristics of the CAK model are retained; for example, there still exists a critical point in the flow, distinct from the sonic point. Also, in this model, as in the CAK model, the critical point is located in the supersonic region of the wind. However, while in the original CAK model it was possible to find exact expressions for the conditions at the critical point of the flow, in this case this is not possible, and an iterative solution is needed. In addition, the nonlocal nature of the problem (in that the flow structure depends on the integrated column density of the wind material N_H), which again is different from previous formulations of the problem, requires an additional iterative loop to find self-consistent dynamical wind solutions.

3.1. The Equation of Motion

In the CAK stellar wind model of an early-type star, the dynamics of the flow is governed by two equations; the angle-dependent mass conservation equation,

$$\frac{d\dot{M}}{d\Omega} = \rho v r^2 , \qquad (9)$$

and the momentum conservation equation,

$$v \frac{dv}{dr} = -\frac{d\Phi}{dr} - \frac{1}{\rho} \frac{dP_g}{dr} + g_R \qquad (10)$$

(see Friend & Castor 1982). In equation (9), $d\dot{M}/d\Omega$ is the mass-loss rate per unit solid angle, Φ is the gravitational potential, P_g is the gas pressure $(= \rho a^2)$, and g_R is the radiative force, given by

$$g_R = \frac{\sigma_e F}{c} K(r, v, dv/dr)M(t, \xi, N_H) , \quad (11)$$

F being the stellar flux (taken from a Kurucz stellar atmosphere model with $T_* = 25,000$ K, $\log_{10} g = 3.0$; Kurucz 1979). The force multipliers $M(t, \xi, N_H)$ are a parameterization of the total radiative line force, and the values calculated in § 2 are used here. In the original formulation of CAK, the force multipliers were a function only of t; here they are a function of t, ξ, and N_H, and this considerably complicates the method of solution. In equation (11), the finite disk correction factor (FDCF) $K(r, v, dv/dr)$ corrects for the finite size of the stellar disk as viewed by stellar wind material (PPK; Stevens 1988b); the calculation of $K(r, v, dv/dr)$ will be discussed in § 3.2.

The gravitational potential $\Phi(r)$ is calculated including the contributions for the two stars; orbital and stellar rotation are, for the sake of simplicity (and to highlight the X-ray ionization effects on the dynamics) not included. Therefore, $\Phi(r)$ is given by

$$\Phi(r) = -GM_* \left[\frac{1 - \Gamma_*}{r} + \frac{q(1 - \Gamma_x)}{D - r} \right], \quad (12)$$

with q defined to be the ratio M_x/M_*, and Γ_* and Γ_x the Eddington ratios for the primary and neutron star, respectively. Substituting equations (9), (11), and (12) in equation (10), the equation of motion then becomes

$$F(r, v, dv/dr) = r^2 \left(v - \frac{a^2}{v} \right) \frac{dv}{dr} - h(r, v, dv/dr)$$
$$- GM_* \Gamma_* K(r, v, dv/dr)M(t, \xi, N_H) = 0 , \quad (13)$$

with

$$h(r, v, dv/dr) = 2a^2 r - r^2 \frac{da^2}{dr} - GM_*$$
$$\times \left[(1 - \Gamma_*) - \frac{q(1 - \Gamma_x)r^2}{(D - r)^2} \right]. \quad (14)$$

The function h is a function of v and dv/dr through its dependence on the temperature and temperature gradient, implicit in the first two terms on the right-hand side of equation (14).

3.2. The Finite-Disk Correction Factor

The FDCF is the ratio of the force multiplier calculated allowing for the finite disk of the star, M_{FD}, to the force multiplier calculated assuming the star is a point source, M. Generalizing the results of CAK to the case in question, the FDCF is given by

$$M_{FD}(t, \xi, N_H) = \frac{2}{1 - \mu_c^2} \int_{\mu_c}^1 M \left[\frac{(1 + \sigma)t}{1 + \sigma\mu^2}, \xi, N_H \right] \mu \, d\mu , \quad (15)$$

with

$$\sigma = \frac{r}{v} \frac{dv}{dr} - 1 \quad (16)$$

and

$$\mu_c^2 = 1 - \left(\frac{R_*}{r} \right)^2 . \quad (17)$$

Using the original CAK approximation for the force multiplier $M(t) = kt^{-\alpha}$, it is possible to get the following analytic expression for the FDCF (for example, see PPK),

$$K(r, v, dv/dr) = \frac{M_{FD}(t)}{M(t)} = \frac{(1 + \sigma)^{1+\alpha} - (1 + \sigma\mu_c^2)^{1+\alpha}}{(1 + \alpha)(1 - \mu_c^2)\sigma(1 + \sigma)^\alpha} . \quad (18)$$

In fact, as mentioned by PPK, the function $K(r, v, dv/dr)$ can be reasonably approximated by ignoring the nonradial terms in equation (18), and thus

$$K(r, v, dv/dr) \sim K(r) = \frac{1 - [1 - (R_*/r)^2]^{1+\alpha}}{(1 + \alpha)(R_*/r)^2} . \quad (19)$$

As discussed by PPK and by Stevens (1988b), this approximation actually gives a very good representation of the effects of the finite-disk factor on the stellar wind dynamics, and indeed this approximation for the FDCF is used in the calculation of the starting approximation for the model (see Appendix).

However, when the CAK approximation for the force multiplier is not used, and the numerical results for $M(t, \xi, N_H)$, obtained in § 2, are used instead, it is not possible to obtain an analytic result for $K(r, v, dv/dr)$. Indeed, in the dynamical calculations presented in the following sections, the numerical results for $M(t, \xi, N_H)$ have been used throughout. In this situation, it is necessary to evaluate the integral in equation (15) numerically to obtain $K(r, v, dv/dr)$. However, this integral is well behaved for the conditions considered in this paper, and its numerical evaluation poses no problem: a simple Simpson's rule method can be used. Results for the calculated form of $K(r, v, dv/dr)$ will be presented in § 4.

3.3. The Method of Solution

The inclusion of X-ray ionization and optical depth effects considerably increases the complexity of the method of solution. In the case of a single star, the force multiplier was a function only of the optical depth parameter t, meaning that the force multiplier depended only on local quantities. Even in the case of the model developed in Paper I, where the force multiplier was a function of both t and ξ, the force multiplier was still a purely local quantity. With the extension to include optical depth effects this is no longer the case, the force multiplier now depending on the integrated column of material in the direction of the neutron star. The outcome of this is that an iterative solution is required. An overall view of the procedure to obtain a self-consistent wind solution is set out below, and the details will be discussed in the subsequent subsections.

As in Paper I, the first step is to transform the equation of motion to a new set of variables, namely, u, w, and w'. As a starting approximation, a guess is made of the critical-point radius r_c (or, correspondingly, u_c); from this guess, initial estimates of the critical-point conditions can be determined using the CAK approximation for the force multiplier (see Appendix). The value of the mass-loss rate found in this way, along with an assumed wind velocity law $[v(r) = v_\infty(1 - R_*/r)^\beta$, with $\beta = 0.8]$, can be used to determine a first approximation for the wind column density from any point in the wind. Next, the critical-point conditions, using the force multipliers calculated in § 2, can then be found by iteration (see § 3.3.2). Then the transformed wind dynamics equation (eq. [25]) can be integrated in both directions from the critical point, to obtain a new wind solution. This solution can then be used to determine a new approximation for the run of column

density. Then the procedure can be repeated using this new approximation for the column density, until both the mass-loss rate and the velocity law converge. In practice, the procedure converges very rapidly, after only 3 or 4 iterations.

3.3.1. Transforming the Equation of Motion

The problem is greatly simplified by the substitution of alternative variables, namely,

$$u = -\frac{2GM_*(1 - \Gamma_*)}{ra_0^2} \tag{20}$$

and

$$w = \frac{v^2}{a_0^2}, \tag{21}$$

where Γ_* is the ratio of the primary luminosity to the Eddington luminosity,

$$\Gamma_* = \frac{\sigma_e L_*}{4\pi GM_* c} \tag{22}$$

and a_0 is the sound speed for material at a temperature equivalent to the effective temperature of the star (T_*). Following on from this,

$$w' = \frac{dw}{du} = \frac{1}{GM_*(1 - \Gamma_*)}\left(r^2 v \frac{dv}{dr}\right). \tag{23}$$

The three dependent variables for the radiative force multiplier, namely, t, ξ, and N_H, also need to be transformed into the new variables u, w, and w', and in particular we find that

$$t = t(w'), \quad \xi = \xi(u, w), \quad N_H = N_H(u). \tag{24}$$

It can be seen that t is a function of w' only, from equations (6), (9), and (23). From equation (1), ξ is a function of both r_x and n; r_x depends solely on u; while from the continuity equation n is a function of both u and w. The method we utilize to get a self-consistent solution means that the column density N_H is only a function of u (§ 3.3.).

With these new variables the equation of motion (13) becomes,

$$F(u, w, w') = \left[1 - \frac{y(u, w)}{w}\right]w' - h(u, w, w')$$

$$- \frac{\Gamma_*}{1 - \Gamma_*} K(u, w, w')M(t(w'), \xi(u, w), N_H(u))$$

$$= 0, \tag{25}$$

with $y(u, w) = (a/a_0)^2 = T/T_*$.

3.3.2. The Critical-Point Conditions

As in the CAK formulation, the equation of motion (25) has a critical point in the supersonic regime of the flow, and, as in CAK, the wind solution must satisfy three conditions at the critical point. First, there is the transformed equation of motion:

$$F(u, w, w') = 0. \tag{26}$$

Second, in the supersonic regime *below* the critical point ($a \leq v \leq v_c$), the equation of motion $F(u, w, w') = 0$ has two positive solutions for w'. The smaller of the solutions for w' is continuous with the solution for w' in the subsonic regime. At the critical point the two roots coincide, and therefore, at the criti-

cal point,

$$\frac{\partial F}{\partial w'} = 0. \tag{27}$$

This equation was termed the *singularity* condition by CAK. Third, considering the full derivative of $F(u, w, w')$,

$$\frac{dF}{du} = \frac{\partial F}{\partial u} + w' \frac{\partial F}{\partial w} + w'' \frac{\partial F}{\partial w'} = 0. \tag{28}$$

Requiring that w'' is finite, and noting that at the critical point $\partial F/\partial w' = 0$, leads to the *regularity* condition,

$$\frac{\partial F}{\partial u} + w' \frac{\partial F}{\partial w} = 0. \tag{29}$$

These three equations, equations (26), (27), and (29), can be used to determine the values of three parameters at the critical point, namely, $d\dot{M}/d\Omega$, w_c, and w'_c. These three values then provide the boundary conditions necessary to integrate the equation of motion, to find a self-consistent solution.

In contrast to the CAK model, when the force multipliers are given by a numerical grid in terms of variables t, ξ and N_H, it is impossible to find a closed analytic form for the critical-point solution, and the solution must be found numerically. However, as a starting point for the numerical solution to the critical-point values, the CAK–type analytic solution is used (see Appendix). Using the values of $d\dot{M}/d\Omega$, w_c, and w'_c determined from the relationships derived in the Appendix, the actual values of these variables that satisfy the three equations above at the critical point can be determined numerically by an iterative procedure.

Substituting for $F(u, w, w')$ in the singularity equation (27) gives

$$\frac{y}{w} + \frac{\partial h}{\partial w'} + \frac{\Gamma_*}{1 - \Gamma_*}\left[\frac{\partial(KM)}{\partial w'}\right] = 0, \tag{30}$$

and substituting for $F(u, w, w')$ into the regularity equation (29) leads to

$$-\left(\frac{w'}{w}\right)\frac{\partial y}{\partial u} - \frac{\partial h}{\partial u} - \frac{\Gamma_*}{1 - \Gamma_*}\left[\frac{\partial(KM)}{\partial u} + w'\frac{\partial(KM)}{\partial w}\right]$$

$$+ y\left(\frac{w'}{w}\right)^2 - \frac{\partial y}{\partial u}w'\left(\frac{w'}{w}\right) - w'\frac{\partial h}{\partial w} = 0. \tag{31}$$

The values of the three relevant critical-point parameters w_c, w'_c, and $d\dot{M}/d\Omega$ can be adjusted until all the conditions of all three equations (26), (30), and (31) are satisfied.

Once the critical-point conditions have been established, it is then possible to integrate the equation of motion using a Runge-Kutta scheme, in both directions from the critical point, using the critical-point conditions as boundary values. As mentioned earlier, it is necessary to iterate to a self-consistent solution. The first iteration to obtain a wind solution is done using a simple approximation to the column density from each point in the wind (see the beginning of § 3.3). Once a wind solution has been obtained, the column density values are then updated using the wind solution just obtained. The procedure is repeated until convergence is obtained.

As a final criterion, the initial guess of the critical radius is adjusted until the electron-scattering optical depth of the wind

is equal to unity:

$$\tau_e = \int_{R_*}^{\infty} \sigma_e \rho \, dr = 1 \, . \qquad (32)$$

This can be achieved by simply varying the initial guess of r_c (or, correspondingly, u_c) until the desired value of τ_e is obtained.

3.4. Effects of Gradients in the Line Force

In the original CAK model the force multipliers are a function of t only, which, when transformed to the new variables (eq. [24]), means that they are a function of w' only. In the present model the force multipliers are a function of u, w, and w'. An important characteristic of line-driven flows which have gradients in the line force with respect to u or w (i.e., $\partial M/\partial u \neq 0$ or $\partial M/\partial w \neq 0$), pointed out first by Vitello & Shlosman (1988), is that there exists an inequality for the line force gradients which, if violated, means that no critical-point solution can be found. Note that Vitello & Shlosman (1988) were considering the case of a wind originating from an accretion disk. There are several important differences between the two situations. The first is that the geometry is different in the two cases; for the accretion disk model the flow is plane-parallel (at least in the regions close to the disk), while in the MXRB model the wind is assumed to be spherically divergent. The second difference concerns the location of the ionizing radiation source; in the accretion disk model the ionizing source is located at the base of the flow, while in the MXRB model considered here the X-ray source is located far out into the flow. Related to this, because of the location of the neutron star, the gravitational potential experienced by wind material will also be very different in the two cases. However, while the geometry and ionization conditions are different, and the derived inequality for the line forces will also be different, the same basic mechanism is at work in both cases.

The influence of line force gradients on the critical-point conditions can be seen by considering the regularity condition (eq. [31]). To a reasonable approximation, close to the critical point $y(u, w) = 1$ and $\partial y/\partial u = \partial y/\partial w = \partial h/\partial w = 0$. This is because no significant temperature variations are taking place close to the critical point, which occurs in the dense region close to the primary star (see §§ 4 and 5). Equation (31) then reduces to

$$\frac{\Gamma_*}{1 - \Gamma_*} \left[\frac{\partial(KM)}{\partial u} + w_c' \frac{\partial(KM)}{\partial w} \right] + \frac{\partial h}{\partial u} - \left(\frac{w_c'}{w_c} \right)^2 = 0 \, . \quad (33)$$

For a stellar wind outflow to exist we must have $dv/dr > 0$ at the critical point (indeed, one of the underlying assumptions of the CAK formalism is of a monotonically increasing wind velocity), and thus for any physically meaningful solution $w_c' > 0$ (from eq. [23] $w' \propto r^2 v \, dv/dr$). Rearranging equation (33) leads to the following inequality relationship for the line force gradients:

$$\frac{\partial(KM)}{\partial u} + w_c' \frac{\partial(KM)}{\partial w} > -\frac{1 - \Gamma_*}{\Gamma_*} \frac{\partial h}{\partial u} \, . \quad (34)$$

Vitello & Shlosman (1988) derived a very similar relationship for the case of winds from accretion disks. For winds from single stars, $\partial h/\partial u > 0$ at the critical point (CAK); however, differentiation and examination of equation (14) reveal that when the effects of a close binary companion are introduced,

$\partial h/\partial u < 0$ at the critical point. Note that Vitello & Shlosman (1988) found that when a nonspherical outflow geometry was assumed for accretion disk winds, $\partial h/\partial u$ was also less than zero.

So in equation (34) $\partial h/\partial u < 0$, and both $\partial K/\partial u$ and $\partial K/\partial w > 0$, while both $\partial M/\partial u$ and $\partial M/\partial w < 0$. The gradients of the FDCF K are reasonably constant with increasing ξ, while those of M increase with increasing ξ (see Fig. 2). Thus, as ξ increases, a point is reached at which inequality (34) can no longer be satisfied, and no critical-point solution is possible. In model results shown in later sections, for both optically thin and thick models, the onset of steep gradients in the line force will provide an upper limit for the neutron star X-ray luminosity for which a wind solution can be found. However, the value of L_x for which this happens will be very different in the two different situations, with the limit for the optically thick case being orders of magnitude larger than for the optically thin case.

4. RESULTS: OPTICALLY THIN MODELS

In the previous two sections we have calculated a grid of radiative force multipliers, and developed a framework to use them to calculate self-consistent one-dimensional models for the wind structure in MXRBs. In this section we show results for the wind of a single early-type star, and for optically thin wind models for MXRBs. In the following section, we present results for the case of optically thick models for MXRBs, which represent the ultimate goal for this paper.

4.1. Single-Star Models

The first application of this model is to the case of a single star, where no X-ray ionization effects are assumed to occur. This case is used as a reference to compare results with the formulation of PPK, as well as the binary models presented later. For the single-star model, the force multipliers for the case of $\xi = 0$ and $N_H = 0$ have been used.

The method of solution presented here is somewhat improved compared with that set out in PPK, in that in the PPK model (as in previous CAK–type models), the force multipliers have been assumed to be represented by a power law in t [i.e., $M(t) = kt^{-\alpha}$, with k and α the CAK constants]. In the method presented here, this assumption is relaxed, and the actual numerical values of $M(t, \xi, N_H)$, which differ from a power law (see Fig. 1), are used.

The assumed stellar parameters used in the calculation are approximately appropriate for the primary star of the MXRB Vela X-1; the stellar mass M_* is 20 $M_\odot$, the stellar radius R_* is 30 $R_\odot$, and as mentioned before, the star is assumed to have an effective temperature of 25,000 K (Conti 1978).

In Figure 4a the velocity law for the single-star model is shown, and in Figure 4b the FDCF is shown. In the supersonic portions of the flow, the wind velocity law, shown in Figure 4a, can be well represented by the formula $v(r) = v_\infty(1 - R_*/r)^\beta$, with $\beta = 0.8$, a result which agrees well with PPK. The terminal velocity for the flow, shown in Figure 4a, is close to $v_\infty = 1200$ km s^{-1}. The form of the FDCF, shown in Figure 4b, is the same as that found by PPK. Close to the primary star $K(r, v, dv/dr) \sim 0.6$, and at the critical point $K = 0.65$. Farther away from the star K becomes greater than unity, peaking at a value of $K \sim 1.02$, at a distance $r \sim 5$–$6R_*$. The mass-loss rate for this model is slightly over 10^{-5} $M_\odot$ yr^{-1}. In Table 1 a summary of these and other derived wind parameters are given, with a comparison to those calculated using a computer
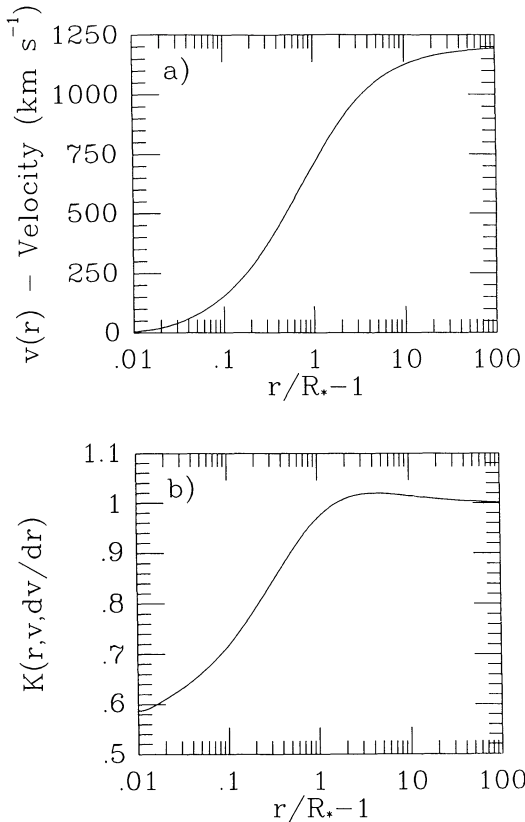
FIG. 4.—Results for a single-star model calculated using the improved model presented in this paper. (a) Wind velocity law $v(r)$. In the supersonic regions of the flow $v(r)$ is well represented by the formula $v(r) = v_\infty(1 - R_*/r)^\beta$ with $\beta = 0.8$. (b) Finite-disk correction factor $K(r, v, dv/dr)$. Further details of the wind solution are given in Table 1.

code developed by the author which uses the PPK method of solution (Stevens 1988b). The values of k and α used in this code (and given in Table 1) are from a least-squares fit to the force multipliers used in these calculations. An important point to note is that a considerable range of mass-loss rate $\dot{M}$ and terminal velocity v_∞ could be obtained from the PPK type code depending on the range in t over which the least-squares fit to obtain k and α was performed. This is simply due to the deviations from a power law of the actual force multipliers. For example, if the power-law approximation over- or underestimates the radiative force multiplier at the critical point, this will directly alter the calculated $\dot{M}$, and this will propagate errors throughout the entire wind solution. Thus great care must be taken to calculate the best-fit values of k and α. It also demonstrates the greater reliability of the method developed

TABLE 1
COMPARISON WITH PREVIOUS RESULTS

Parameter	This Paper	PPK
k	...	0.32
α	...	0.64
$\dot{M} (10^{-6} M_\odot \text{ yr}^{-1})$	11.62	10.01
$v_\infty (\text{km s}^{-1})$	1197	1160
$r_c (R_\odot)$	1.049	1.061
$v_c (\text{km s}^{-1})$	75.5	82.7
$v_* (\text{km s}^{-1})$	0.58	0.50

here, which does not rely on a power-law fit but uses the calculated force multipliers directly.

From Table 1 it can be seen that the calculated wind parameters for the model star are similar to those for the primary of Vela X-1. The mass-loss rate is somewhat higher compared with the observed value of $\dot{M}_{\text{obs}} = 7 \times 10^{-6} M_\odot \text{ yr}^{-1}$, and the terminal velocity somewhat lower than the observed value $v_\infty = 1500 \text{ km s}^{-1}$ (Conti 1978). Considerably better agreement between the observed wind parameters for Vela X-1 and the calculated values could have been obtained by varying the assumed values of M_* and R_*, within the observed range of possible values. Given that we are not attempting a detailed model of Vela X-1, but only investigating the general behavior of systems such as Vela X-1, this is sufficient for the purposes of this paper.

4.2. Optically Thin Models for MXRBs

The next step is to calculate models for MXRB systems, where X-ray ionization effects are included but optical depth effects are neglected. For these models the separation of the system is assumed to be $2R_*$ (cf. MV), and the neutron star mass is taken to be the canonical value of $M_x = 1.4 M_\odot$. The stellar surface is assumed to be held fixed at $R_* = 30 R_\odot$ and not perturbed by the gravitational field of the neutron star. In previous two-dimensional models, the surface of the primary has been assumed to follow an equipotential surface (e.g., Friend & Castor 1982; Stevens 1988a). For the one-dimensional models presented here, this comprises an unnecessary complication, and the neglect of tidal distortion implies no loss of generality.

The optically thin MXRB models presented here are very similar to those discussed in Paper I, and are included here for completeness and for purposes of comparison with the optically thick models presented in the following section. Paper I should be referred to for a more complete discussion of optically thin models.

The calculated velocity laws for three different values of the X-ray luminosity are shown in Figure 5, which shows the region from the surface of the primary star (at $r = 30 R_\odot$) to the neutron star (at $r = 60 R_\odot$). Also, additional information
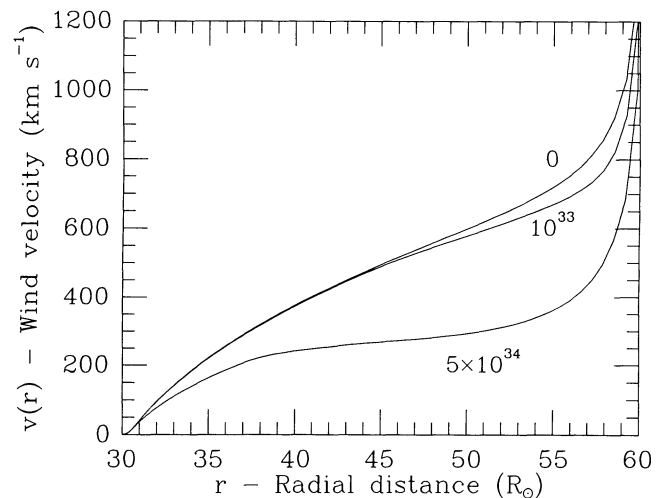

FIG. 5.—Wind velocity laws for three optically thin MXRB models. The curves are labeled with the respective values of the neutron star X-ray luminosity L_x. The neutron star is assumed to lie at a distance $D = 60 R_\odot (= 2R_*)$.

TABLE 2

RESULTS FOR OPTICALLY THIN WIND MODELS

L_x (ergs s^{-1})	r_c (R_*)	$\log_{10} \xi_c$	$d\dot{M}/d\Omega$ (10^{-7} $M_\odot$ yr^{-1} sr^{-1})	v_c (km s^{-1})	$v(r = 1.5R_*)$ (km s^{-1})
0	1.051	...	10.11	72.0	491.0
10^{33}	1.052	-3.52	9.89	72.6	489.5
5×10^{34}	1.090	-1.56	8.86	100.6	267.2

on the models is given in Table 2. Clearly, the influence of X-ray ionization is to suppress the wind acceleration, leading to significantly smaller velocities (reducing the wind velocity by up to 50% at some radial distances). However, from Table 2, X-ray ionization has a considerably smaller effect on the mass-loss rate, with $\dot{M}$ only declining by ~ 12% for the model with the highest X-ray luminosity.

The reason for this behavior is as follows; in the low-velocity (subcritical) regime, the density is high and the ionization parameter ξ correspondingly low, and the suppression in the radiative force is minimal. Thus, the wind mass-loss rate, which is determined by the conditions at the critical point, is largely unchanged, and also the wind velocity is largely unaffected in these regions close to the primary star. However, in the supersonic regime the ionization parameter rises sharply and the dynamical effects increase. X-ray ionization tends to decrease the radiative force, and thus tends to decrease the wind acceleration and the wind velocity compared with the case of no X-ray ionization. From Table 2, and Figure 5 for the case of $L_x = 5 \times 10^{34}$ ergs s^{-1}, the wind velocity in the supersonic regime can be suppressed to a velocity of around 200 km s^{-1} over large radial distances. Close to the neutron star, the gravitational force from the neutron star dominates the flow dynamics completely, and the wind material in all models is gravitationally accelerated to high velocities.

In their models, MV found that, for a certain range of X-ray luminosities, both the mass-loss rate and the wind velocities could be enhanced. The calculations presented here do not reproduce this result and suggest that the maximum mass-loss rate and wind velocity occur for zero X-ray luminosity, and any increase in X-ray luminosity will decrease both the mass-loss rate and the wind velocity in the supersonic regime. This is likely due to the fact that MV included the contribution of only a few lines to the radiative driving of the wind material in their model. When a much larger assemblage of lines is used, as is the case here, the influence of an individual line on the dynamics is much suppressed. As the X-ray ionization increases, and the wind material becomes increasingly ionized, the general trend is for the radiative force multiplier to decrease with increasing ξ. While strong lines from more highly ionized species, such as N V $\lambda 1240$ or O VI $\lambda 1032$, do start significantly contributing to the force multiplier at higher values of ξ, this is always more than offset by the decline in the radiative force from less ionized species which tend to disappear with increasing ξ. Also, the nature of the radiative force in a supersonic wind naturally tends to limit the force contribution from an individual line (see Paper I for more details).

For values of $L_x \geq 5 \times 10^{34}$ ergs s^{-1} no solution could be found that satisfies all the critical-point conditions. This is because of the increasing gradients in the radiative line force, namely, $\partial M/\partial u$ and $\partial M/\partial w$. As described in § 3.4, there exists a limit for the gradients in the line force at the critical point beyond which no critical-point solution is possible. As noted

earlier, the mass-loss rate is not strongly affected by X-ray ionization (see Fig. 2). However, the gradients of the force multiplier, $\partial M/\partial u$ and $\partial M/\partial w$, are more sensitive to ξ. For the optically thin case, the magnitudes of the gradients begin to increase quite significantly around $\log_{10} \xi \sim -1.5$, and, as they increase, eventually it becomes impossible to find a solution.

In summary, for optically thin models, X-ray ionization has a relatively small effect on the mass-loss rate from the primary but can have a significant impact on the wind velocity law in the supersonic regime, potentially suppressing the wind velocity by a factor of 2 in some instances. As a consequence of this and mass conservation, the density can be enhanced by nearly a factor of 2 in certain regimes of the flow, and this could potentially have consequences for the attenuation of the observed X-ray flux (see § 6). The suppression of the wind velocity in the supersonic regime also will have some very important consequences for the mass accretion rate on the neutron star (which is a very sensitive function of the wind velocity) and the resultant level of X-ray emission. This also will be discussed later within the context of the optically thick models. However, it must be noted that the values of L_x for these models are significantly lower than those observed for Vela X-1. This discrepancy will also be addressed in the following section.

5. RESULTS: OPTICALLY THICK MODELS

The model results presented in this section are for the same binary parameters as in § 4, and once more the X-ray luminosity of the neutron star is used as a free parameter. The difference this time is that now the effects of a finite optical depth are included in the models, and, as described in § 3, an iterative solution is now required to obtain self-consistent model solutions.

From Figures 1 and 2, the introduction of optical depth effects tends to diminish the influence of X-rays on the force multipliers. For example, for a value of $N_H = 10^{22}$ cm^{-2}, at $\log_{10} \xi = 0$, the force multiplier has decreased by only a small amount (~ 5%), whereas for the optically thin case, at $\log_{10} \xi = 0$, the force multiplier has decreased by almost an order of magnitude. Thus, qualitatively speaking, the introduction of optical depth effects should allow wind solutions at significantly higher values of L_x than for the optically thin case, bringing the models more in line with the observations of MXRBs.

In Figure 6 the wind velocity profiles for a number of models are plotted, and in Table 3 additional information on these models is given. The basic characteristics of the variation of the wind velocity law with ξ for the optically thick case, shown in Figure 6, are quite similar to those shown in Figure 5, for optically thin models. Close to the primary, the wind velocity is largely unaffected, as is the mass-loss rate. However, in the supersonic regime, major suppression of the wind velocity is
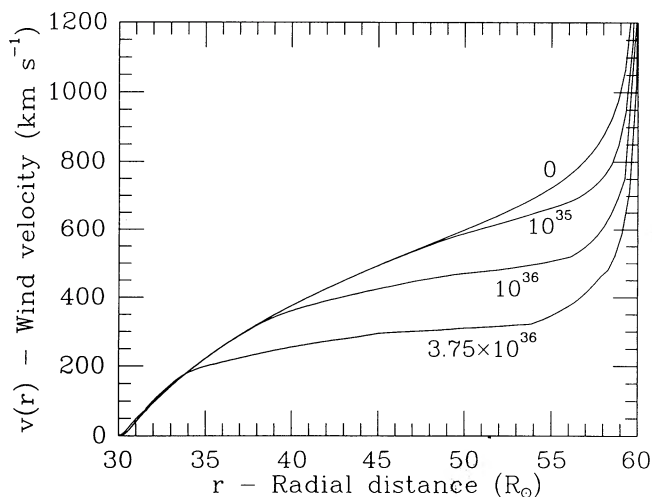
FIG. 6.—Wind velocity laws for four optically thick wind models for MXRBs. The curves are labeled with the respective values of the neutron star X-ray luminosity L_x. The neutron star is assumed to lie at a distance $D = 60$ $R_\odot$ ($= 2R_*$). Note, that in comparison to the optically thin models, shown in Fig. 5, the value of L_x to achieve the same degree of reduction in the wind velocity is approximately two orders of magnitude higher.
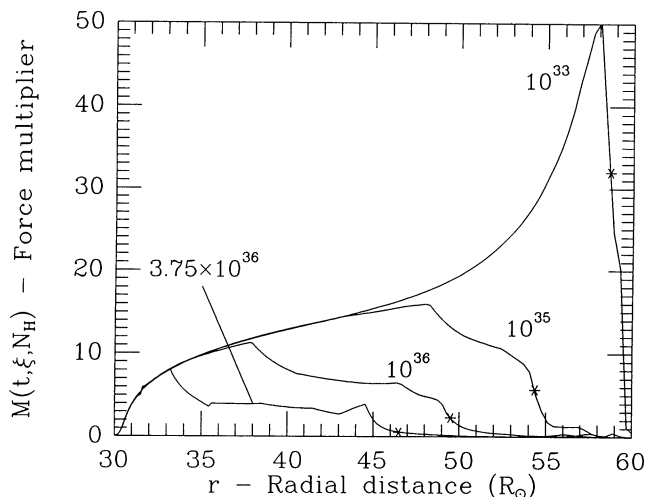

FIG. 7.—Radiative force multiplier $M(t, \xi, N_H)$ as a function of radial distance r for four different optically thick MXRB models, with the value of the neutron star X-ray luminosity used as a free parameter. The curves are labeled with their respective values of L_x. The location of the helium edge for each model is also marked (asterisks).

seen for values of $L_x \geq 10^{36}$ ergs s^{-1}. The most important difference between the results shown in Figures 5 and 6 is that, for the optically thick models, the X-ray luminosities required to produce the same behavior are roughly two orders of magnitude higher than in the optically thin case. For the case of $L_x = 3.75 \times 10^{36}$ ergs s^{-1}, the wind velocity is held below 300 km s^{-1} for a large part of the supersonic regime. Again, close to the neutron star, the gravitational force of the neutron star dominates the flow, and the wind is accelerated to high velocities. As mentioned earlier, the mass-loss rate remains quite insensitive to changes in the X-ray luminosity, decreasing by only around 5% as L_x varies from 0 to 3.75×10^{36} ergs s^{-1}, with the maximum mass-loss rate occurring for the case of no X-ray ionization. In the optically thin models, the value of ξ_c was always small ($\log_{10} \xi_c \leq -1.5$; see Table 2), and the force multiplier was essentially unchanged by X-ray ionization. From Table 3 we see that for the optically thick models much higher values of ξ_c are allowed ($\xi_c \sim 1$ for $L_x = 3.75 \times 10^{36}$ ergs s^{-1}). However, because the critical point is located close to the primary star ($r_c \sim 1.05R_*$), the column density of attenuating material is very high ($N_H \sim 3 \times 10^{23}$ cm^{-2}), and the radiative force multiplier is still very similar to its values in the limit of no X-ray ionization (see Fig. 2). The decreased wind velocity in the supersonic regime and the mass-loss rate being essentially held constant lead to the wind being significantly denser in the supersonic regime for the models with higher values of L_x, and the ratio of the densities of the model with

$L_x = 3 \times 10^{36}$ ergs s^{-1} to that with $L_x = 0$ is greater than 2 in certain portions of the supersonic flow.

As in the optically thin case, increasing gradients in the force multiplier with respect to u and w eventually mean that as L_x increases there eventually comes a point where no critical-point solution can be found. However, optical depth effects postpone this point to values of $L_x \sim 4 \times 10^{36}$ ergs s^{-1} (cf. § 3.4).

In Figure 7 the variation of the radiative force multiplier $M(t, \xi, N_H)$ with radial distance is shown for the same four models illustrated in Figure 6. From Figure 7 we can see that the force multipliers are largely unaffected in the dense low-velocity regimes near the primary star. This explains the relative invariance of the stellar mass-loss rate with increasing X-ray ionization (see above). However, Figure 7 also shows graphically how quickly the force multiplier drops in the super-sonic region, for the higher values of L_x. For the model with $L_x = 10^{33}$ ergs s^{-1}, close to the primary, and throughout a major portion of the supersonic region, $M(t, \xi, N_H)$ rises steadily in a manner similar to that for a single-star model (cf. PPK), the X-ray luminosity for this model being sufficiently low so as not to have a major impact on the wind dynamics, until very close to the neutron star (see Fig. 9). However, close to the neutron star, the force multiplier is subject to two competing effects. First, the gravitational force of the neutron star tends to accelerate the material; this leads to a higher velocity gradient, which, because the force mulipliers $M(t, \xi, N_H)$ calculated in

TABLE 3
RESULTS FOR OPTICALLY THICK WIND MODELS

L_x (ergs s^{-1})	r_c (R_*)	$\log_{10} \xi_c$	$d\dot{M}/d\Omega$ (10^{-7} $M_\odot$ yr^{-1} sr^{-1})	v_c (km s^{-1})	$v(r = 1.5R_*)$ (km s^{-1})	L_x^{out} (ergs s^{-1})
0	1.051	...	10.11	72.1	494.8	1.62×10^{35}
10^{33}	1.051	-3.53	10.04	71.8	492.5	2.00×10^{35}
10^{34}	1.052	-2.53	9.98	71.8	492.3	2.40×10^{35}
10^{35}	1.052	-1.53	9.92	71.5	493.0	3.59×10^{35}
10^{36}	1.050	-0.55	9.87	68.2	423.9	1.04×10^{36}
3.75×10^{36}	1.046	0.024	9.65	67.5	294.1	3.89×10^{36}

this paper still retain the basic characteristic of the CAK force multipliers—that $M(t, \xi, N_H) \propto (dv/dr)^\alpha$ with $\alpha > 0$—finally results in the radiative force being enhanced (see Fig. 1).

Physically, the reason for the dependence of the force multiplier on the velocity gradient is as follows. Consider a monotonic accelerating wind, and a strong spectral line at a frequency ν_0. At a certain location in the wind, at a radial distance r with a velocity v, because of the Doppler shift of the wind material, the spectral line will have absorbed the stellar flux between the frequencies ν_0 and $\nu = \nu_0(1 + v/c)$. If some external factor were to increase the velocity gradient at this radial distance r (such as the gravitational force of a companion star), this would lift the material out of the "shadow" of the underlying material, exposing it to continuum radiation, and thus lead to an enhanced radiative force. On the other hand, if some external mechanism were to reduce the velocity gradient at the radial point r (such as X-ray ionization), then this would tend to keep the wind material within the "shadow" of the underlying material, and thus reduce the radiative force (see below).

The second effect concerns the decrease in the radiative force associated with increasing ionization. For the model with $L_x = 10^{33}$ ergs s^{-1}, the decrease in $M(t, \xi, N_H)$ with increasing ξ only becomes important very close to the neutron star. Thus, for this model, the radiative force first begins to rise sharply as the gravitational force of the neutron star accelerates the material, which in turn feeds back to further accelerate the material, and then $M(t, \xi, N_H)$ drops sharply as the X-ray ionization quickly extinguishes the radiative force. For the other models, with higher X-ray luminosities, both effects described above are still at work. However, because the X-ray flux is higher in these cases, the gravitationally enhanced feedback mechanism for the radiative force multiplier does not play a large role, and the reduction in the force multiplier caused by X-ray ionization dominates. Figure 7 further illustrates that the decline in the force multiplier is not a sharp cutoff as has been assumed by other authors (Ho & Arons 1987; Blondin et al. 1990). Earlier we showed that the decline in the force multiplier was associated with the He II–He III ionization edge. However, Figure 7 shows that the reduction in $M(t, \xi, N_H)$ is not just limited to the region close to the ionization edge, and significant decline in $M(t, \xi, N_H)$ occurs in the He II region. For the models with higher values of L_x this is particularly marked, the force multiplier having dropped by an order of magnitude at the helium edge. Some of this is directly due to the decrease of $M(t, \xi, N_H)$ with ξ, seen earlier, but another factor that causes the decline in the radiative force is the nonlinearity of the dynamical equations. Small decreases in the force multiplier can feedback, causing further reductions in the force multiplier, a reduction in $M(t, \xi, N_H)$ leading to a reduction in the velocity gradient, leading to a greater reduction in $M(t, \xi, N_H)$ (see above).

In Figure 8 the relationship between the ionization parameter ξ and the column density N_H is plotted for four optically thick models. Close to the primary star, ξ will be small and N_H will be large, while close to the neutron star the situation will be reversed. For higher values of L_x the location of a point with a certain value of ξ will be preferentially closer to the primary star than for a model with lower L_x, and the value of the attenuating column density N_H will be higher. From Figure 8 we see that the column density of attenuating material is extremely large for the major part of the flow, and reveals the extent of the departure from the optically thin case. Also plotted in Figure 8 is the location of the helium ionization edge
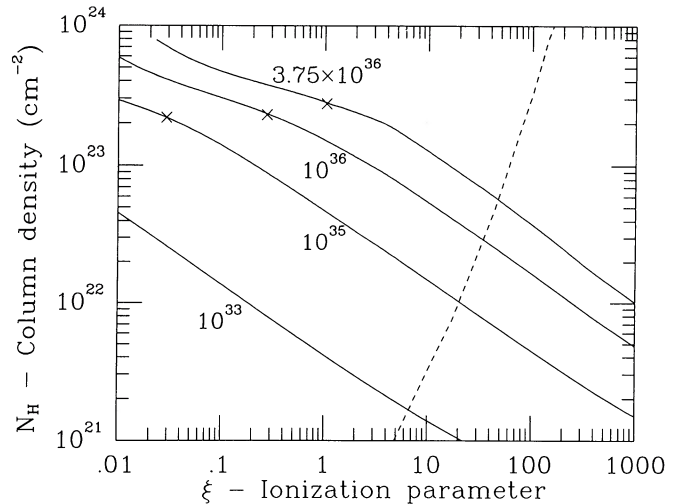

FIG. 8.—Relationship between the ionization parameter ξ and the column density N_H for three optically thick models, labeled with their respective value of the neutron star X-ray luminosity L_x (solid lines). The locations of the critical points for the models are also marked (crosses). Also plotted is the location of the helium ionization front as a function of ξ and N_H calculated in § 2.3 (dashed line).

in the (ξ, N_H)-plane. Thus the intersection of this line with the results for the calculated models indicates the location of the helium ionization front for each model. The helium ionization edge provides a reasonable estimate of the location where the radiative force becomes negligible. As we have seen from Figure 7, the radiative force does not cutoff sharply at this edge, but its location provides a useful scale height for the model. Of note, for the higher luminosity models, is that the location of the ionization edge is restricted to a relatively small range in ξ. For the model with $L_x = 3.75 \times 10^{36}$ ergs s^{-1} the ionization edge occurs at $\log_{10} \xi = 1.65$, while for the model with $L_x = 10^{35}$ ergs s^{-1} the ionization edge still occurs at $\log_{10} \xi = 1.32$, a factor of 2 change in ξ for close to a factor of 40 change in L_x.

In Figure 9 the variation of the ionization parameter ξ as a function of radial distance r is shown, also for the same four models described in previous figures. Also plotted is the location of the helium ionization edge. The location of this edge moves steadily toward the primary star with increasing L_x, and for the model with $L_x = 3.75 \times 10^{36}$ ergs s^{-1} it is close to the midpoint of the flow.

5.1. The Mass Accretion Rate

In the above discussion of both optically thin and optically thick models for MXRB systems, the neutron star X-ray luminosity L_x has been used as a free parameter. In reality, the X-ray luminosity of the system is determined by the accretion rate onto the neutron star, which in turn depends on system parameters (binary separation, stellar masses, binary period), as well as wind parameters (mass-loss rate, velocity law). Thus, the wind characteristics and the X-ray luminosity of MXRBs represent a highly coupled system. In this section we investigate the possibility of finding self-consistent solutions for the X-ray luminosity and wind dynamics. While all the calculations presented above have been for one-dimensional models, looking solely at the dynamics along the line of centers of the system, it is possible to use these results to get an estimate of the mass accretion rate $\dot{M}_{acc}$. If we neglect the Coriolis force (Friend & Castor 1982), then only material that is relatively
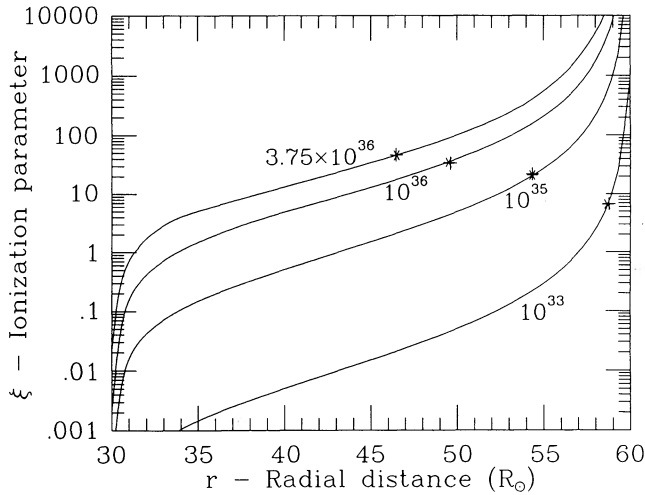
FIG. 9.—Radial variation of the ionization parameter ξ, for four optically thick models, with the neutron star X-ray luminosity L_x as the free parameter (curves are labeled with L_x). The location of the helium ionization edge, defined to be the location where the abundances of He II and He III are equal, is also marked for each of the four models (asterisks).

close to the line of centers of the system (typically within a few degrees) will be accreted onto the neutron star. Thus, even though the mass-loss rate and the wind velocity structure vary as a function of angle from the line of centers, because we are considering only small departures (of the order of a few degrees) we can, to a reasonable approximation, use the conditions on the line of centers to obtain an estimate of the mass accretion rate onto the neutron star.

The mass-accretion rate onto the neutron star will then be given by

$$\dot{M}_{\rm acc} = \frac{\pi r_a^2}{D^2} \frac{d\dot{M}}{d\Omega} , \qquad (35)$$

with $d\dot{M}/d\Omega$ being the angular mass-loss rate along the line of centers and r_a the accretion radius, given by

$$r_a = \frac{\alpha_{\rm BH} G M_x}{v_w^2 + v_{\rm orb}^2} ; \qquad (36)$$

v_w is the wind speed, $v_{\rm orb}$ is the orbital velocity of the neutron star (which for the system parameters used is equal to approximately 260 km s^{-1}), and $\alpha_{\rm BH}$ is the "Bondi-Hoyle" accretion constant. The value of this constant is usually assumed to be $\alpha_{\rm BH} = 2$ (Bondi & Hoyle 1944). However, more recent numerical simulations (for example, Shima et al. 1985; Blondin et al. 1990) have found that in the very complex gas flows that occur in MXRBs, the value of $\alpha_{\rm BH}$ used in equation (36) departs from this value, and to account for this we calculate the mass accretion rate assuming three values of $\alpha_{\rm BH}$, namely, $\alpha_{\rm BH} = 1$, 1.4, and 2. Note that the value $\alpha_{\rm BH} = 1.4$ has been recently suggested by the work of Blondin, Stevens, & Kallman (1991). Note also that the numerical simulations of Blondin et al. (1991) demonstrate that the mass accretion rate will be a strongly time-dependent quantity, varying quite rapidly on short time scales, and the value of $\alpha_{\rm BH}$ assumed will provide a time-averaged measure of the mass accretion rate. However, equations (35) and (36) should provide an adequate representation of the time-averaged accretion rate, and the discussion presented here should be a good representation of the time-averaged properties of MXRBs.

The resultant X-ray luminosity from this accretion is then given by

$$L_x^{\rm out} = \zeta \dot{M}_{\rm acc} c^2 , \qquad (37)$$

with ζ an efficiency factor usually taken to be 0.1 for neutron stars (McCray 1977). We can use the dynamical models calculated in the previous section to obtain an estimate of the accretion radius r_a (the value of which depends quite strongly on the assumed value of $\alpha_{\rm BH}$), and from this an estimate of the mass accretion rate (eq. [36]), and finally the resultant X-ray luminosity. There are now two relevant values of the X-ray luminosity for each model. The first is the value of the X-ray luminosity that was used as an input parameter in the models calculated in the previous section (here we shall term this parameter $L_x^{\rm in}$), and the second is the accretion driven X-ray luminosity calculated from equation (37), termed $L_x^{\rm out}$. For a self-consistent model, clearly we require that $L_x^{\rm in} = L_x^{\rm out}$.

In Figure 10, for the three values of $\alpha_{\rm BH}$, the relationship between the model input X-ray luminosity $L_x^{\rm in}$ and the resultant X-ray luminosity $L_x^{\rm out}$ is plotted. While for each value of $\alpha_{\rm BH}$ there are some important differences, the general trend is the same. At small values of $L_x^{\rm in}$, $L_x^{\rm out} > L_x^{\rm in}$. As $L_x^{\rm in}$ increases, $L_x^{\rm out}$ increases as well, at first somewhat less than linearly, but at higher values of $L_x^{\rm in}$ approximately linearly. This increase in $L_x^{\rm out}$ is due to the changing wind dynamics. As shown in Figure 6, as $L_x^{\rm in}$ increases, the wind velocity is suppressed, which in turn increases the accretion radius, and thus $\dot{M}_{\rm acc}$ and $L_x^{\rm out}$. When $\alpha_{\rm BH} = 2$, for which case the accretion radius and $L_x^{\rm out}$ are the greatest, there are no self-consistent solutions, and $L_x^{\rm out} > L_x^{\rm in}$ for all $L_x^{\rm in}$. In contrast, for the case where $\alpha_{\rm BH} = 1$, where the accretion radius and $L_x^{\rm out}$ are the smallest, there is one distinct solution, at a value of $L_x \sim 2 \times 10^{35}$ ergs s^{-1}. The most interesting case is for the intermediate value of $\alpha_{\rm BH} = 1.4$. In this case, the condition $L_x^{\rm out} = L_x^{\rm in}$ is satisfied (to within a few percent) for a range of L_x between 10^{36} and 3.75×10^{36} ergs s^{-1}. Thus, if we assume that $\alpha_{\rm BH} = 1.4$, there exists a range of possible self-consistent solutions for our MXRB model, with an X-ray luminosity in the range of a few times 10^{36} ergs s^{-1}, a
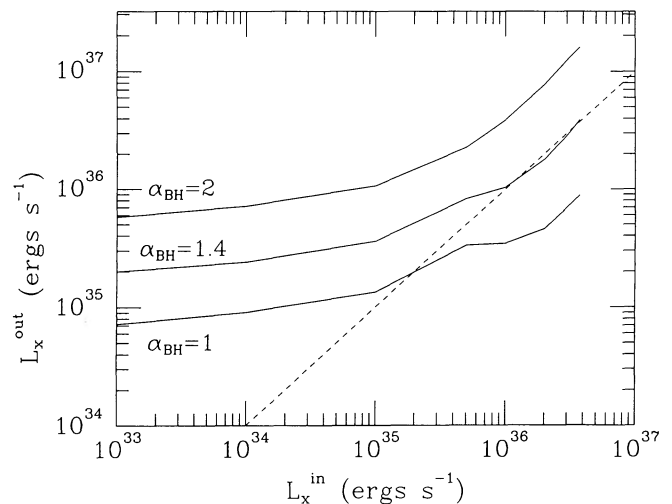

FIG. 10.—Relationship between the value of the X-ray luminosity $L_x^{\rm in}$, which is used as an input parameter in the models calculated in § 5, and $L_x^{\rm out}$, which is the X-ray luminosity calculated from the model results. Results are plotted for three different values of the "Bondi-Hoyle" accretion constant $\alpha_{\rm BH}$ (solid lines). For ease of reference, the case when $L_x^{\rm in} = L_x^{\rm out}$ is also plotted (dashed line).

value which is similar to that actually observed for Vela X-1 (White et al. 1983). Note that this level of self-consistency suggested by Figure 10 should be treated with caution, in that these calculations have attempted insight by means of a one-dimensional model of what is fundamentally a three-dimensional problem. Also, MXRBs are seen to be strongly variable at X-ray wavelengths, meaning that the accretion rate is also time-dependent. While the above calculations do give insight into the interaction of radiation and matter in an MXRB, the fact that a self-consistent solution is found for a range of values of L_x should only be taken to indicate some sort of general time-averaged behavior.

These results, therefore, give rise to the possibility that the effect of X-ray ionization on the wind dynamics in MXRBs can give rise to the existence of a number of stable X-ray states that an MXRB could exist in. A similar conclusion was reached by Ho & Arons (1987) in their MXRB model, although the fact that we were unable to find dynamical solutions for values of $L_x \geq 4 \times 10^{36}$ ergs s^{-1} precludes any discussion about the existence of very high X-ray luminosity discussed by Ho & Arons (1987).

6. DISCUSSION

In the previous sections we have developed the necessary tools to calculate realistically the dynamics of an X-ray–illuminated wind in a MXRB system, including the influence of X-ray ionization on the wind dynamics, and accounting for the influence of attenuation of the X-rays from the neutron star. For parameters suitable for the MXRB system Vela X-1, we have found self-consistent dynamical solutions, with X-ray luminosities consistent with those observed for Vela X-1. These results represent a considerable improvement over previous attempts to model MXRB winds self-consistently, where X-ray luminosities were obtained which were orders of magnitude below those observed (cf. MV; Paper I); the important difference being that these papers did not include optical depth effects in the calculation of the radiative force.

We have shown in § 2 the sensitivity of the force multipliers to both the ionization parameter ξ and the attenuating column density N_H. Increasing ξ tends to reduce $M(t, \xi, N_H)$, while increasing N_H has the opposite effect. The He II–He III ionization edge marks the location where the force multiplier drops rapidly to zero. However, it is important to note that the force multipliers drop gradually in the He II region, and that the decline in $M(t, \xi, N_H)$ with increasing ξ is certainly not a step function, with a sharp cutoff at the helium ionization edge.

In the optically thick dynamical models calculated in § 5, X-ray ionization does not seriously alter the subsonic velocity structure or the mass-loss rate of the primary star. The main impact is on the supersonic wind velocity, which can be severely reduced by X-ray ionization. This decrease in the wind velocity, coupled with the mass-loss rate being largely unchanged, means that the density in an X-ray–illuminated wind will be higher than that of an undisturbed wind, by up to a factor 2 for some locations and X-ray luminosities. However, this is likely unrelated to the absorption dips seen in MXRBs (Charles et al. 1978), which are more likely associated with some form of accretion wake, as shown in the numerical simulations of Blondin et al. (1990).

Also of note is the nonlinearity of the dynamical equations, with various feedback mechanisms, which can either further enhance or suppress the radiative force, depending on what additional mechanism is at work. This is because of the dependence of the force multiplier on the local wind velocity gradient, and this means that under certain conditions, relatively small changes in the ionization structure can result in fairly major changes in the wind dynamics (§ 5). Also, in these models the radiative force is suppressed over a large part of the supersonic flow, and there is no sharp cutoff in the radiative force.

In their two-dimensional numerical simulations Blondin et al. (1990) sought to include the effect of X-ray ionization on the wind dynamics by including a force cutoff. For values of ξ less than a certain critical value the radiative force was unaffected, while for values larger than this the radiative force was set to zero. Blondin et al. (1990) set this cutoff to occur at $\log_{10} \xi = 2.5$. However, as we have noted above, the force multipliers do not behave in such a well-mannered way, the decline with respect to ξ being more gradual and complicated.

An obvious future improvement on this work would be to utilize the force multiplier calculations presented here in conjunction with a two-dimensional time-dependent model, such as that of Blondin et al. (1990). Simulations such as those of Blondin et al. (1990) are needed to study the complex time-dependent behavior of MXRBs, and have revealed a wealth of interesting phenomena, such as ionization wakes, accretion wakes, and short-lived disklike accretion phenomena. It is therefore desirable to find a means of combining the results presented in this paper with models such as that of Blondin et al. (1990), to understand whether the phenomena found in that paper will still be apparent when more realistic approximations are employed for the effect of X-rays on the wind dynamics.

As noted earlier with regard to Figure 8, the location of the helium ionization edge is relatively restricted in terms of ξ; as L_x varies from 10^{35} to 3.75×10^{36} ergs s^{-1}, the location of the edge moves from $\log_{10} \xi = 1.65$ to $\log_{10} \xi = 1.32$. Comparison of Figures 7 and 9 also reveals that the location of the point where the radiative force begins to drop sharply is also quite localized in terms of ξ, near a value of $\log_{10} \xi \sim 1$–1.5. Thus, calculations of the sort described by Blondin et al. (1990) performed with a force cutoff located at around $\log_{10} \xi = 1$–1.5 would probably represent a reasonable first approximation to the results presented here. However, the inclusion of the force cutoff would also eliminate many of the nonlinear feedback effects found associated with the dynamical models shown in § 5.

The accretion rate onto the neutron star is a sensitive function of the wind velocity law $\dot{M}_{acc} \propto v^{-4}$, and because X-ray ionization can alter v by a factor of 2 or more, the assumed X-ray luminosity for the model can change the value of $\dot{M}_{acc}$ by an order of magnitude or more. Ho & Arons (1987), in their one-dimensional analytic approach, adopted a similar force cutoff to that described for the Blondin et al. (1990) model. Typically, Ho & Arons (1987) found that their MXRB models could exist in two self-consistent luminosity states, one high- and one low-luminosity state. In the low-luminosity state, the wind was largely unaffected by X-rays until very close to the neutron star. Note that Ho & Arons (1987) set the radiative force cutoff to occur at $\log_{10} \xi = 4$, a value which is at least two orders of magnitude too high (see Fig. 2). In this case the wind velocity at the radius of the neutron star would be large, leading to small X-ray luminosity ($L_x \sim 10^{35}$ ergs s^{-1}). In contrast, in the high-luminosity state, the wind material would be ionized by the X-ray source while still close to the surface of the primary, and would then coast at low speed before being accreted, leading to a very high luminosity ($\sim 10^{38}$ ergs s^{-1}).

However, in the high-luminosity state there are several important assumptions that tend to undermine the applicability of their results. In particular, in the high-luminosity models, the radiative force cutoff occurs very close to the primary star, and the wind material coasts at a velocity typically less than the orbital speed, which means that the neglect of the Coriolis force will likely be important. Also, Ho & Arons (1987) assumed a value of $\xi_{cut} = 10^4$. If a more realistic, smaller value of ξ_{cut} were used, the force cutoff would occur even closer to the primary star, and at even lower velocities, and the neglect of the Coriolis force will be even more important. Also, the neglect of X-ray heating, and the one-dimensional nature of their formulaton, mean that the actual wind structure is likely to be considerably more complicated than suggested by the model of Ho & Arons (1987).

The dynamical results presented in § 5 somewhat change this picture of a simple force cutoff, and a dichotomy of two solutions, one high- and one low-luminosity. Assuming parameters appropriate for Vela X-1, we found a range of possible self-consistent solutions, ranging from values of L_x of 10^{36} to 3.75×10^{36} ergs s^{-1}. Even at these values of L_x the wind velocity is strongly affected by X-ray ionization. Unfortunately, because of difficulties intrinsic to the CAK formulation, we are unable to say anything about the wind structure in the case when the X-ray luminosity is very high.

One a more speculative note, from the point of view of the wind dynamics in MXRBs, it may be possible to split the class into three broad (and probably not very well defined) categories. At the lowest X-ray luminosities, the Be/X-ray binaries (which numerically comprise the largest subtype of MXRBs) in quiescence have X-ray luminosities with $L_x \sim 10^{32}$–10^{33} ergs s^{-1} (van den Heuvel & Rappaport 1986). These systems are powered by the weak winds from the Be star primaries. In this situation, where wind densities (and column densities) are low, the optically thin results presented in § 4 will likely be applicable. For the classical MXRBs which have moderate luminosities ($L_x \sim 10^{35}$–10^{37} ergs s^{-1}), such as Vela X-1 and 4U 1700−37, the optically thick calculations presented in this paper will likely be appropriate. However, for the very high

luminosity systems ($L_x \geq 10^{38}$ ergs s^{-1}), such as SMC X-1, LMC X-4, and possibly Cen X-3, the model presented here will probably not work. As seen in § 5, in the one-dimensional models presented in this paper, there is an upper limit to the value of L_x for which solutions can be found. Also, in these systems other important mechanisms will be at work and must be included in any realistic model of such a system. For example, the X-ray flux in these systems is so strong that the primary star will be strongly irradiated, possibly leading to a strong self-excited evaporative wind from the primary (London, McCray, & Auer 1981). Also, because the material will likely be very ionized over a large volume, and thus presumably flowing quite slowly (there being little radiative driving of the wind material), two-dimensional effects associated with the Coriolis force or binary rotation will likely be much more important than in the moderate X-ray luminosity systems primarily considered in this paper.

In conclusion, we have calculated a series of MXRB models accounting for the influence of X-rays on the wind dynamics, and including optical depth effects in the transfer of X-rays from the neutron star through the wind material. The force multipliers are found to be a very sensitive function of the column density N_H as well as the ionization parameter ξ. Dynamical models, using parameters appropriate for Vela X-1, calculated using these results reveal a number of nonlinear feedback mechanisms that affect the wind dynamics, whereby relatively small changes in the force multipliers can lead to large changes in the wind structure. The models also find the existence of a self-consistent region of solution at X-ray luminosities $\sim 10^{36}$ ergs s^{-1}, in agreement with the observed value of L_x for Vela X-1.

APPENDIX

As a starting point to find the critical-point solution when the numerical grid of values of $M(t, \xi)$ is used, the three equations, that define the critical-point conditions (namely, the equation of motion, the singularity condition, and the regularity condition, eqs. [26], [27], and [29], respectively) are solved using a power-law expression for $M(t)$ and ignoring any temperature or ionization effects. Using

$$M(t) = kt^{-\alpha} , \tag{A1}$$

and noting that

$$t = \left(\frac{\sigma_e v_{th} \, d\dot{M}/d\Omega}{GM_*(1 - \Gamma_*)} \right) w' , \tag{A2}$$

then the equation of motion becomes

$$F(u, w, w') = \left(1 - \frac{1}{w}\right) w' - h(u) - CK(u, w, w')(w')^\alpha , \tag{A3}$$

with

$$C = \frac{\Gamma_*}{1 - \Gamma_*} \left[\frac{GM_*(1 - \Gamma_*)}{\sigma_e v_{th} \, d\dot{M}/d\Omega} \right]^\alpha \tag{A4}$$

STEVENS

This equation can then be substituted in the three conditions at the critical point, and neglecting any nonradial terms in $K(u, w, w')$ (see text for a further explanation of this), the following expressions can be found:

$$w'_c = B_1^{1/2} - \frac{\alpha h(u)}{1 - \alpha},$$ (A5)

$$w_c = 1 - \frac{\alpha h(u)}{(1 - \alpha)B_1^{1/2}},$$ (A6)

with

$$B_1 = \frac{dh}{du} - \frac{h}{1 - \alpha}\frac{1}{K}\frac{dK}{du}.$$ (A7)

This leads to the following expression for the mass-loss rate:

$$\frac{d\dot{M}}{d\Omega} = \frac{GM_*(1 - \Gamma_*)}{\sigma_e v_{\text{th}}}\left[\frac{\Gamma_* k}{(1 - \Gamma_*)C}\right]^{1/\alpha},$$ (A8)

with

$$C = -\frac{h}{1 - \alpha}\frac{1}{K}(w'_c)^{-\alpha}.$$ (A9)

These values for $d\dot{M}/d\Omega$, w_c, and w'_c are then used to determine the critical-point conditions when X-ray heating and X-ray ionization are included in the dynamics.

REFERENCES

Abbott, D. C. 1982, ApJ, 259, 282
Blondin, J. M., Kallman, T. R., Fryxell, B. A., & Taam, R. E. 1990, ApJ, 356, 591
Blondin, J. M., Stevens, I. R., & Kallman, T. R. 1991, ApJ, 371, 684
Bondi, H., & Hoyle, F. 1944, MNRAS, 104, 273
Cassinelli, J. P., & Swank, J. H. 1983, ApJ, 271, 681
Castor, J. I., Abbott, D. C., & Klein, R. I. 1975, ApJ, 195, 158 (CAK)
Charles, P. A., Mason, K. O., White, N. E., Culhane, J. L., Sanford, P. W., & Moffatt, A. F. J. 1978, MNRAS, 183, 813
Conti, P. S. 1978, A&A, 63, 225
Corcoran, M., & Heap, S. 1991, ApJ, submitted
Drew, J. E. 1989, ApJS, 71, 267
Dupree, A. K., et al. 1980, ApJ, 238, 969
Friend, D. B., & Abbott, D. C. 1986, ApJ, 311, 701
Friend, D. B., & Castor, J. I. 1982, ApJ, 261, 293
Haberl, F., White, N. E., & Kallman, T. R. 1989, ApJ, 343, 409
Hatchett, S., Buff, J., & McCray, R. 1976, ApJ, 206, 847
Hatchett, S., & McCray, R. 1977, ApJ, 211, 552
Ho, C., & Arons, J. 1987, ApJ, 316, 283
Howarth, I. D., & Prinja, R. K. 1989, ApJS, 69, 527

Kallman, T. R., & McCray, R. 1982, ApJS, 50, 263
Kurucz, R. L. 1979, ApJS, 40, 1
London, R., McCray, R., & Auer, L. 1981, ApJ, 243, 970
MacGregor, K. B., & Vitello, P. A. 1982, ApJ, 259, 267 (MV)
Masai, K. 1984, Ap&SS, 106, 391
McCray, R. 1977, Highlights Astr., 4, 155
McCray, R., Kallman, T. R., Castor, J. I., & Olson, G. L. 1984, ApJ, 282, 245
Pauldrach, A., Puls, J., & Kudritzki, R. P. 1986, A&A, 164, 86 (PPK)
Prinja, R. K., & Howarth, I. D. 1988, ApJS, 61, 357
Shima, E., Matsuda, T., Takeda, H., & Sawada, K. 1985, MNRAS, 217, 367
Stevens, I. R. 1988a, MNRAS, 232, 199
———. 1988b, MNRAS, 235, 523
Stevens, I. R., Blondin, J. M., & Kallman, T. R. 1990, BAAS, 21, 1206
Stevens, I. R., & Kallman, T. R. 1990, ApJ, 365, 321 (Paper I)
van der Heuvel, E. P. J., & Rappaport, S. 1986, in IAU Colloquium 92, Physics of Be Stars, ed. A. Slettebak & T. D. Snow (Cambridge: Cambridge Univ. Press)
Vitello, P. A., & Shlosman, I. 1988, ApJ, 327, 680
White, N. E., Swank, J. H., & Holt, S. S. 1983, ApJ, 270, 711